

Testing Lorentz invariance of dark matter with satellite galaxies

Dario Bettoni^a Adi Nusser^b Diego Blas^c Sergey Sibiryakov^{c,d,e}

^aInstitut für Theoretische Physik, Ruprecht-Karls-Universität Heidelberg
Philosophenweg 16, 69120 Heidelberg, Germany

^bPhysics Department and the Asher Space Science Institute - Technion, Haifa 32000, Israel

^cTheoretical Physics Department, CERN, CH-1211 Geneva 23, Switzerland

^dInstitute of Physics, LPPC, Ecole Polytechnique Fédérale de Lausanne, CH-1015 Lausanne, Switzerland

^eInstitute for Nuclear Research of the Russian Academy of Sciences, 60th October Anniversary Prospect, 7a, 117312 Moscow, Russia

E-mail: d.bettoni@thphys.uni-heidelberg.de, adi@physics.technion.ac.il,
diego.blas@cern.ch, sergey.sibiryakov@cern.ch

Abstract. We develop the framework for testing Lorentz invariance in the dark matter sector using galactic dynamics. We consider a Lorentz violating (LV) vector field acting on the dark matter component of a satellite galaxy orbiting in a host halo. We introduce a numerical model for the dynamics of satellites in a galactic halo and for a galaxy in a rich cluster to explore observational consequences of such an LV field. The orbital motion of a satellite excites a time dependent LV force which greatly affects its internal dynamics. Our analysis points out key observational signatures which serve as probes of LV forces. These include modifications to the line of sight velocity dispersion, mass profiles and shapes of satellites. With future data and a more detailed modeling these signatures can be exploited to constrain a new region of the parameter space describing the LV in the dark matter sector.

Keywords: Cosmology: large scale structure of the Universe, dark matter theory, Lorentz violation, galaxy dynamics

ArXiv ePrint: [1702.07726](https://arxiv.org/abs/1702.07726)

Contents

1	Introduction	1
2	Lorentz violating dark matter	2
3	The weak-field and non-relativistic limit	3
4	Lorentz violation in dark matter halos	4
4.1	Equations of motion in the satellite frame of reference	5
4.2	Solution to the Aether equation	6
4.2.1	Solution for a single halo	7
4.2.2	A satellite in a halo	8
4.2.3	Comparison with gravitational forces	9
4.3	Numerical results	10
4.3.1	Particle distribution	13
4.3.2	Radial mass profiles	14
4.3.3	Mass extraction	16
4.3.4	Ellipticity	17
5	Discussion and conclusions	19
A	analytic solution for the LV vector	21

1 Introduction

The evolution of the Universe and the observed cosmic structures is well embraced by the Λ CDM model [1]. The model is based on General Relativity (GR) with a cosmological constant term and on the matter content provided by Standard Model (SM) plus a dark matter (DM) component. One of the fundamental pillars of such construction is the assumption of Lorentz Invariance of the underlying theory. This requirement has far reaching consequences for both gravitational interaction and the construction of the SM. Indeed, Lorentz symmetry is one of the most solid and tested symmetries, with extremely tight experimental constraints in both the gravitational and particle physics sectors [2–7].

Certain theories of quantum gravity involve some degree of Lorentz violation (LV) [8–10] which, despite originating at high energy, may have significant consequences on all scales [11]. The absence of Lorentz Invariance is also the basis for interesting proposals for dark energy [12, 13] and inflation [14–16]. It is hence worthwhile to explore the observable signatures of LV on the dynamics of the low energy sector of the theory. There is no unique recipe for breaking Lorentz Invariance. We consider here a specific, yet well-motivated [10, 17, 18], choice where a vector degree of freedom takes a time-like non vanishing vacuum expectation value, effectively breaking the Lorentz group. The most general action for such an LV vector was derived in [17] and its astrophysical implications have been widely investigated [19–21] (for a recent review on the phenomenology of LV theories see [22]).

Once new degrees of freedom are present, it is natural to consider their coupling to other particles, unless some mechanism prevents them or make them negligible. The constraints

on these interactions are very strong for SM particles [4] (see [23] for a general framework to parameterize LV extension of SM). However, there are currently few and less stringent constraints on couplings of LV fields to the DM sector. A first investigation in this direction was undertaken in [24, 25] where the theory is checked against the large scale structures and cosmic Microwave Background radiation (CMB). The effect of LV is twofold. First, it results in breaking of the Weak Equivalence Principle (WEP) by modifying the inertial mass of DM particles without an equal compensation in the gravitational mass. Second, it introduces a non-trivial velocity dependent interaction.

In this paper we explore consequences of LV on smaller, non-linear, scales. As we shall see, small scales structures probe a completely different range of the model parameters. Indeed, the effects introduced by the LV vector are screened above a certain parameter-dependent scale implying that there may be significant modifications on small scales while the evolution on large scales remains essentially intact [25]. Hence, the investigation of non-linear structures opens up a window on unexplored values of parameters.

Our aim is to offer a broad assessment of the possible effects of the coupling between DM and the LV vector on small scales. In particular, we will be interested in the consequences of such coupling on the dynamics of DM dominated satellite galaxies orbiting inside significantly more massive host halos. Using this type of systems, we will define characteristic observable features that can be used to constrain the LV models. Satellites and galaxies have been exploited in the literature for testing breaking of the WEP in the dark sector [26–29]. Although the LV theory we consider here also generates WEP violation, the main focus is on specific aspects of LV.

A full N-body simulation would be required in order to assess the exact level of LV effects in realistic scenarios. This is a formidable numerical effort which is beyond the scope of the current paper. Instead we resort to a semi-analytic approach which describes idealized situations. The approach helps preparing the ground for a more complex analysis, by pointing to promising paths for further explorations.

The paper is organized as follows. In section 2 we introduce the model and we recall some previous results while in section 3 we discuss the weak field regime which serves as a basis for the subsequent discussion. In section 4 we focus in the implications of LV for DM halos. Section 4.1 describes the relevant equations for DM particles, while Section 4.2 presents the solutions of the LV field in the halos and useful insights into the physics of Lorentz-violating dark matter (LVDM). In section 4.3 we present the results of the numerical integration of the dynamics and, finally, in section 5 we summarize the observational tests for the LVDM model and draw our conclusions. Appendix A contains some analytic solutions.

2 Lorentz violating dark matter

We will assume that the Universe is endowed with a preferred time direction or foliation of space-time that breaks Lorentz invariance. This can be described by introducing the ‘Aether’ vector U^μ and forcing it to have a time-like unit norm that selects the preferred time direction. The most general low-energy action that describes the dynamics of this theory is the so called Einstein–Aether (\mathcal{A}) action [17, 30] and is given by

$$S_{\text{IR}} = -\frac{M_0^2}{2} \int d^4x \sqrt{-g} (R + K^{\alpha\beta}{}_{\mu\nu} \nabla_\alpha U^\mu \nabla_\beta U^\nu + \lambda(U^\mu U_\mu - 1)), \quad (2.1)$$

where λ is a Lagrangian multiplier enforcing the unit norm of the vector U^μ , M_0 is a scale related to the Planck mass [22] and

$$K^{\alpha\beta}{}_{\mu\nu} = c_1 g^{\alpha\beta} g_{\mu\nu} + c_2 \delta_\mu^\alpha \delta_\nu^\beta + c_3 \delta_\nu^\alpha \delta_\mu^\beta + c_4 U^\alpha U^\beta g_{\mu\nu}. \quad (2.2)$$

The dimensionless parameters c_i characterize the interaction between the LV vector and gravity. The strongest constraints on these couplings come from Solar system physics through the post-Newtonian (PPN) parameters [2] $\alpha_1^{\text{PPN}} \leq 10^{-4}$ and $\alpha_2^{\text{PPN}} \leq 4 \cdot 10^{-7}$, which generically imply [31] $|c_i| < 10^{-7}$. However, the Solar System bounds can be satisfied by specific combinations of the couplings, which still yield part of the parameter space totally unconstrained. The latter can be explored through other observations, as Big Bang Nucleosynthesis (BBN) [32], dynamics of binary systems [20, 21], or linear cosmology [25].

The bounds on possible direct couplings of SM to the \mathcal{A} -field are very tight [4, 6] and can be safely assumed to be zero for astrophysical and cosmological implications. Hence, broken Lorentz symmetry will affect ordinary matter only via gravitational interaction. This assumption can be relaxed in the case of DM. Since the relation between DM and SM particles remains uncertain, there is no solid reason to expect that their couplings to the LV sector may be of the same order. From this point of view, the study of LV in the DM sector offers a new handle in testing one of the most fundamental paradigms of modern physics, with important consequences for quantum gravity.

We thus equip the \mathcal{A} theory with an explicit coupling between the LV vector and DM which will break the Lorentz invariance of this component. This is achieved by modifying the action for a DM particle as follows [24]

$$S_{\text{dm}} = -m \int ds F(U^\mu \mathcal{V}_\mu / c), \quad (2.3)$$

where $ds \equiv \sqrt{g_{\mu\nu} dx^\mu dx^\nu}$, $\mathcal{V}^\mu \equiv dx^\mu / ds$ is the particle's four-velocity and F is an arbitrary positive function normalized in such a way that $F(1) = 1$.

The sum of the two actions (2.1) and (2.3), plus any other minimally coupled matter species, defines the LVDM model whose small scales dynamics will be now investigated.

3 The weak-field and non-relativistic limit

The dynamics of DM halos can be accurately described by the weak-field and non-relativistic limit of the action presented in the previous section. This is achieved by first expanding the action (2.1) together with (2.3) around flat space to second order in the fields. We decompose the metric as $g_{00} = 1 + 2\phi$, $g_{i0} = 0$ and $g_{ij} = -\delta_{ij}(1 - 2\psi)$ and the vector field as $U^\mu = \delta_{\mu 0} + u^\mu$. Assuming non-relativistic velocities for the particles and that the time derivatives of the potentials are sub-leading, the weak field action reads

$$S = \frac{M_0^2}{2} \int d^4x (4\phi \nabla^2 \psi - 2\psi \nabla^2 \psi + \kappa_A \mathbf{u} \cdot \nabla^2 \mathbf{u} + \kappa_B (\partial_i u^i)^2) + \int d^4x \rho \left[\frac{\mathbf{V}^2}{2c^2} - \phi - \frac{Y}{2} \left(\mathbf{u} - \frac{\mathbf{V}}{c} \right)^2 \right], \quad (3.1)$$

where we defined $Y = F'(1)$, $\kappa_A \equiv c_1$ and $\kappa_B \equiv c_2 + c_3$; and introduced $V^i = dx^i / dt$ and the DM density $\rho = m \sum_A \delta^{(3)}(x - x_A)$. Notice that this action is invariant under Galilean transformations that act on the velocity and Aether by a constant shift

$$\mathbf{V} \mapsto \mathbf{V} + \mathbf{v}_0, \quad \mathbf{u} \mapsto \mathbf{u} + \frac{\mathbf{v}_0}{c}.$$

In what follows we mostly focus on the choice of parameters with $\kappa_B = 0$. This is a well defined effective theory which simplifies our analysis and still yields an interesting phenomenology. It is also favored by some theoretical arguments [33]. The most general case will be considered in future work.

In the special case of negligible Aether fluctuations ($u^i = 0$) the DM action is

$$S_{pp} = \int d^4x \rho \left[(1 - Y) \frac{\mathbf{V}^2}{2} - \phi \right], \quad (3.2)$$

which shows that the inertial and gravitational masses are not equivalent anymore and the Equivalence Principle is not satisfied. This introduces a segregation between DM and baryons which in our scenario are not affected by LV¹. The last term in the action (3.1) gives rise to a quadratic potential for the Aether inside regions with non-zero DM density. The stability of the Minkowski background requires this potential and the effective inertial mass of DM particles to be positive, which implies $0 < Y < 1$ [24]. The potential tends to align the Aether vector \mathbf{u} with the DM velocity leading to a suppression of LV effects on the dynamics (screening mechanism).

Variations of (3.1) with respect to the matter velocity \mathbf{V} , the LV vector \mathbf{u} and the gravitational potentials ϕ and ψ yield the equations of motion,

$$\frac{1 - Y}{c^2} \frac{dV^i}{dt} + \partial_i \phi + \frac{Y}{c} \left(\frac{du^i}{dt} + (cu^j - V^j) \partial_i u^j \right) = 0, \quad (3.3)$$

$$\Delta u^i = \frac{8\pi G Y \rho}{c^2 \kappa_A} \left(u^i - \frac{\bar{V}^i}{c} \right), \quad (3.4)$$

$$\Delta \phi = \frac{4\pi G}{c^2} \rho, \quad \psi = \phi. \quad (3.5)$$

Since DM is collisionless, in the derivation of (3.4) we allow for multiple streams each with its own velocity existing at a certain point. Therefore, the equation involves the (mass weighted) mean particle velocity \bar{V}^i . Equation (3.5) is the standard Poisson equation, meaning that the LV vector \mathbf{u} does not modify the relation between the gravitational potential and the mass density. In addition, DM obeys mass conservation as described by the usual continuity equation.

4 Lorentz violation in dark matter halos

Internal dynamics of DM halos are a plausible testbed of the direct coupling of the LV field to DM. Inside the virial radius of a halo, matter is in near dynamical equilibrium and overlapping streams of particles moves in random directions. Thus, in the reference frame moving with the bulk motion of the halo, the mean particle velocity, $\bar{\mathbf{V}}$, is very close to zero. Since \mathbf{u} is sourced by $\bar{\mathbf{V}}$ through (3.4), an individual particle moving with a random velocity $\mathbf{V} \neq \bar{\mathbf{V}}$ will always experience an LV force through the term $c\mathbf{u} - \mathbf{V}$ in (3.3).

Still, the internal dynamics of an isolated halo moving with a *constant* bulk velocity is not significantly affected by LV. To see this, let us perform a Galilean boost to the frame moving with the halo. In this frame the LV vector is time-independent. Hence, the action

¹In fact it is enough that they have different Y parameter; we assume $Y_b = 0$.

for the DM particles does not involve any terms which depend explicitly on time, resulting in an “energy-like” conserved quantity. This can be demonstrated by multiplying the velocity equation (3.3) by \mathbf{V} to obtain

$$\frac{1-Y}{2c^2} \frac{d\mathbf{V}^2}{dt} = -\mathbf{V} \cdot \nabla \left(\phi + \frac{Y}{2} \mathbf{u}^2 \right). \quad (4.1)$$

This equation implies that the quantity

$$\mathcal{E} = \frac{1-Y}{2c^2} \mathbf{V}^2 + \phi + \frac{Y}{2} \mathbf{u}^2 \quad (4.2)$$

is an integral of motion. Although the LV force still affects the halo dynamics, this conservation law prevents any significant departures from the standard evolution governed by gravity alone.

The time independence is broken for satellite halos orbiting inside a more massive host halo. The orbital motion of these satellites introduces a time dependent LV vector which breaks the conditions for the conserved quantity above. We will consider two types of systems. The first one is intended to mimic a dwarf satellite galaxy in the halo of the Milky Way (MW). Most of these satellites are DM dominated, with baryons having only a modest effect on their overall dynamical evolution. The second system is a galaxy in a massive cluster. This system is three orders of magnitude more massive than the first galactic system and probes a different velocity regime of the LV force (see below). We work with an idealized configuration as summarized schematically in Fig. 1.

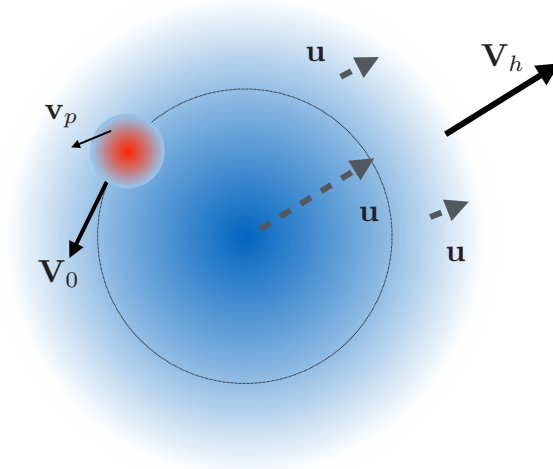


Figure 1. Schematic representation of the satellite and the host halo system. A spherical host halo is moving with constant velocity \mathbf{V}_h relative to the CMB frame. $\mathbf{V}_0 = \mathbf{V}_s - \mathbf{V}_h$ is the bulk velocity of the satellite (subhalo) relative to the host halo. $\mathbf{v}_p = \mathbf{V} - \mathbf{V}_s$ is the relative velocity of a particle with respect to the subhalo velocity. The vector \mathbf{u} vanishes outside of the host halo (it vanishes in the CMB frame) and is aligned with \mathbf{V}_h at small scales due to a screening mechanism (see (3.4) and (4.10)).

4.1 Equations of motion in the satellite frame of reference

We write the equations of motion of particles belonging to a satellite bound to a host halo as shown in Fig. 1. The distance of a particle from the center of the satellite is denoted by r .

Furthermore, let us denote by M_v and r_v the virial mass and virial radius of the satellite (the latter is defined as the radius inside which the average density is 200 times the background value). The actual mass and radius of the satellite will be denoted by M_s and r_s , respectively. Due to tidal disruption by the gravitational field of the parent halo, r_s is smaller than r_v . We also define $V_c = (GM_s/r_s)^{1/2}$ as the circular velocity of a baryonic tracer moving in a circular orbit at $r = r_s$ under the action of gravity alone.

Substituting in (3.3) $\mathbf{v}_p = \mathbf{V} - \mathbf{V}_s$ for the velocity of a particle in a frame of reference moving with velocity \mathbf{V}_s with respect to the CMB frame yields the modified Euler equation,

$$(1 - Y) \frac{d\tilde{v}_p^i}{d\tau} + \frac{c^2}{V_c^2} \tilde{\partial}_i \phi_{sat} + \left(\frac{d\tilde{V}_s^i}{d\tau} + \frac{c^2}{V_c^2} \tilde{\partial}_i \phi_h \right) + Y \left[\frac{d(\tilde{u}^i - \tilde{V}_s^i)}{d\tau} + (\tilde{u}^j - \tilde{V}_s^j - \tilde{v}_p^j) \tilde{\partial}_i \tilde{u}^j \right] = 0, \quad (4.3)$$

where ϕ_h and ϕ_{sat} are, respectively, the gravitational potentials generated by the host and satellite halos. We have introduced the rescaled variables

$$\tilde{x}^i = x^i/r_{sc}, \quad \tau = tV_c/r_{sc}, \quad \tilde{u}^i = cu^i/V_c, \quad \tilde{V}^i = V^i/V_c, \quad \tilde{\partial}_i = \partial/\partial\tilde{x}^i = r_{sc}\partial/\partial x^i. \quad (4.4)$$

Here

$$r_{sc} = \sqrt{\frac{c^2 \kappa_\Lambda}{8\pi G(1 + \delta_v)Y\bar{\rho}}} = 1.43 \text{ Gpc} \sqrt{\left(\frac{10}{1 + \delta_v}\right) \left(\frac{0.3}{\Omega_0}\right) \left(\frac{\kappa_\Lambda}{Y}\right) \frac{70 \text{ (km/s)/Mpc}}{H_0}}, \quad (4.5)$$

where² $1 + \delta_v \approx 200/3$ is the DM overdensity at the virial radius, $\bar{\rho} = 3H_0^2\Omega_0/(8\pi G)$ is the average DM density in the Universe, H_0 is the Hubble constant and Ω_0 is the present day DM background density parameter. As we will see shortly, r_{sc} marks the screening length, above which the LV force is suppressed.

\mathbf{V}_s is identified as the velocity of the satellite's central particle ($r = 0$) and we consider parameters for which \mathbf{u} is aligned with \mathbf{V}_s at the core of the satellite so that the LV force on the central particle vanishes (see discussion in appendix A). Then the central particle follows the same trajectory as it would have under the influence of gravity alone. Moreover, we will neglect the tidal gravitational forces exerted on the satellite by the host halo, as we want to isolate the effect of the LV interactions. In this approximation the combination in the round brackets in (4.3) is zero and we obtain,

$$(1 - Y) \frac{d\tilde{v}_p^i}{d\tau} = -\frac{c^2}{V_c^2} \tilde{\partial}^i \phi_{sat} - Y \left[\frac{d(\tilde{u}^i - \tilde{V}_s^i)}{d\tau} + (\tilde{u}^j - \tilde{V}_s^j - \tilde{v}_p^j) \tilde{\partial}_i \tilde{u}^j \right]. \quad (4.6)$$

This form of the equation will be used in numerical simulations.

4.2 Solution to the Aether equation

We turn now to equation (3.4) which determines the LV vector \mathbf{u} from the density and the velocity fields. We consider cases where the radius of the satellite and the screening length are much smaller than the radius of the host halo. Therefore, as far as the internal dynamics of the satellite is concerned, we can treat the host halo as an infinite medium with constant density. We also assume that the satellite is spherical. Equation (3.4) can be rewritten in a dimensionless form,

$$\tilde{\Delta} \tilde{u}^i = \frac{\rho(r)}{\rho(r_v)} (\tilde{u}^i - \tilde{V}^i), \quad (4.7)$$

²The precise value of $1 + \delta_v$ depends on the halo profile. It is equal to 200/3 for the halo density $\rho \propto r^{-2}$.

where ρ is the mass density profile and $\rho(r_v)$ is the mass density of the satellite at the virial radius, cf. (4.5). Given that the Poisson equation (3.5) is linearly sourced only by the matter density, it can be easily integrated. Note that if the typical variation of the density occurs on scales larger than r_{sc} , equation (4.7) implies $\tilde{\mathbf{u}} = \tilde{\mathbf{V}}$. Then, in the case of a single stream, i.e. $\mathbf{v}_p = 0$, equation (4.3) would reduce to the standard Euler equation with the LV force screened away [24]. In the general case of multiple streams, particles that do not move with the average velocity are affected by the LV force. Still, the Euler equation is recovered upon averaging over the whole set of particles.

We can now solve equation (4.7) in the two cases that are relevant for our investigation. First, we will solve it for a single halo with a time independent velocity. The aim in this case is to find the conditions on the parameters r_{sc} for which the inner part of such halo is unaffected by the LV force, i.e. the situation where screening is efficient. Secondly, we will study what happens in the case of a satellite orbiting around its host halo in the case of screening happening in the latter. A detailed derivation of the solutions is provided in appendix A.

4.2.1 Solution for a single halo

Consider the idealized situation of a DM halo, described as a sphere of constant density, moving with a constant bulk velocity \mathbf{V}_h with respect to the CMB frame. Recall that for any virialized object the average velocities of the particles inside it is zero. In this case the equation (4.7) reads,

$$\tilde{\Delta}\tilde{u}^i = (\tilde{u}^i - \tilde{V}_h^i) \quad \text{for } r \leq r_h, \quad (4.8)$$

$$\tilde{\Delta}\tilde{u}^i = \alpha^2\tilde{u}^i \quad \text{for } r \geq r_h, \quad (4.9)$$

where r_h is the physical radius of the halo and $\alpha^2 = \rho_{\text{out}}/\rho_{\text{in}}$ is the ratio between the density outside and inside the halo. Note that in this case ρ_{in} coincides with the virial density of the halo. We take the solution to be continuous at $r = r_h$ together with its first derivatives. We obtain that Aether vector is directed along \mathbf{V}_h and has the following radial dependence

$$\begin{aligned} \mathbf{u}_{\text{in}}(r) &= \frac{\mathbf{V}_h}{c} \left[1 - \frac{(r_h + r_0) \sinh(r/r_{sc})}{\sinh(r_h/r_{sc}) r} \right], \\ \mathbf{u}_{\text{out}}(r) &= -\frac{\mathbf{V}_h r_0}{c r} e^{-\alpha(r-r_h)/r_{sc}}, \end{aligned} \quad (4.10)$$

where r_0 is a constant fixed by matching the solution at $r = r_h$ and we have restored physical units.

The solution (4.10) has three regimes, depending on the ratio r_h/r_{sc} : If $r_h/r_{sc} \gg 1$, the variation of u occurs abruptly close to the edge of the halo (very efficient alignment). In this case, only a thin shell experiences the LV force. Throughout the interior of the halo ($r < r_h$), the effects of LV are almost vanishing because $\mathbf{u} \rightarrow \mathbf{V}_h/c = \text{const}$. In the case $r_h/r_{sc} \ll 1$ the variation of the LV vector \mathbf{u} over the size of the halo is very small and the force given by the last term in equation (3.3) is negligible. Thus, the only consequence of LV in this case is the difference between the inertial and gravitational masses. Finally, the velocity-dependent LV force is relevant in the cases where $r_{sc} \sim r_h$, which means that particles inside the halo will experience a force which depends on their position. Figure 2 shows solutions for the three cases.

For our investigation of the dynamics of the subhalo we will focus on the case $r_{sc} \ll r_h$, for which the LV effects of the host halo are screened and can be ignored. In Fig. 2 we see

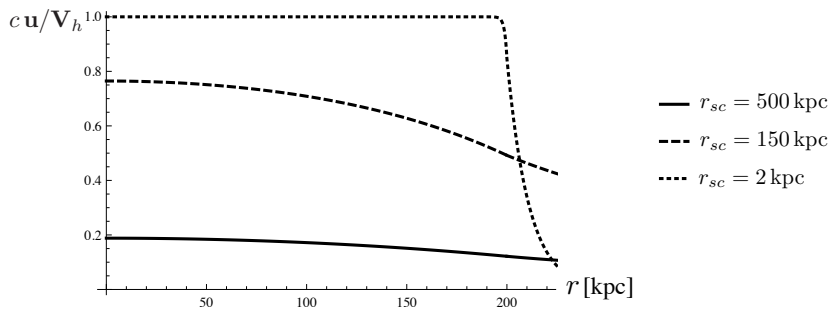


Figure 2. Solution of the inner region for various values of r_{sc} of 2 kpc, 150 kpc and 500 Mpc. The radius of the halo is taken to be $r_h = 200$ kpc, corresponding to the virial radius of the Milky Way while $\alpha = 0.1$.

that $r_{sc} \leq 0.01 r_h$ is sufficiently small to guarantee a negligible LV force inside the halo. For an MW-like halo, this corresponds to $r_{sc} \sim 1 - 10$ kpc and the LV effects of the external halo can be ignored as long as the subhalo is not close to the edge. For example, the Draco dwarf is at a distance of $r_{\text{Draco}} \sim 80$ kpc, whereas the virial radius of the MW is $r_{\text{MW}} \sim 200$ kpc [34]. We find that at Draco’s distance, even a value as high as $r_{sc} \sim 50$ kpc suppresses LV effects of the parent halo.

4.2.2 A satellite in a halo

We now turn to the dynamics of a DM satellite orbiting in its host halo. The host is assumed to have a constant velocity \mathbf{V}_h with respect to the CMB and the satellite to move with velocity $\mathbf{V}_0 = \mathbf{V}_s - \mathbf{V}_h$ with respect to the host halo (see Fig. 1). We work in a frame of reference whose origin, $r = 0$, coincides with the center of the satellite. The vector \mathbf{u} is the solution to the general equation (4.7) with the following source,

$$\begin{aligned} \mathbf{V}(r) &= \mathbf{V}_s & \text{for } r \leq r_s, \\ \mathbf{V}(r) &= \mathbf{V}_h & \text{for } r > r_s, \end{aligned} \quad (4.11)$$

where r_s is the radius of the satellite. We assume that the satellite is spherically symmetric with $\rho \propto r^{-2}$ (see appendix A for the solution in the case of a more general density profile containing a core). In terms of the scaled variables (4.4) the Aether equation reads,

$$\tilde{\Delta} \tilde{u}^i = \left(\frac{\tilde{r}_v}{\tilde{r}} \right)^2 (\tilde{u}^i - \tilde{V}_s^i) \quad \text{for } \tilde{r} \leq \tilde{r}_s, \quad (4.12)$$

$$\tilde{\Delta} \tilde{u}^i = \alpha_h^2 (\tilde{u}^i - \tilde{V}_h^i) \quad \text{for } \tilde{r} > \tilde{r}_s, \quad (4.13)$$

where $\alpha_h^2 = \rho_h / \rho_s(r_v)$ is the ratio between the halo density and the virial density of the satellite. Notice that we assume a host halo of constant density. The solution to the previous system of equations is

$$\tilde{\mathbf{u}}(\tilde{r}) - \tilde{\mathbf{V}}_s = \frac{\tilde{\mathbf{V}}_h - \tilde{\mathbf{V}}_s}{1 + \frac{n}{1 + \alpha_h \tilde{r}_s}} \left(\frac{\tilde{r}}{\tilde{r}_s} \right)^n \equiv -\tilde{\mathbf{V}}_0 w_{in}(\tilde{r}) \quad \text{for } \tilde{r} \leq \tilde{r}_s, \quad (4.14)$$

$$\tilde{\mathbf{u}}(\tilde{r}) - \tilde{\mathbf{V}}_s = (\tilde{\mathbf{V}}_h - \tilde{\mathbf{V}}_s) \left[1 - \frac{n}{n + 1 + \alpha_h \tilde{r}_s} \frac{\tilde{r}_s}{\tilde{r}} e^{-\alpha_h(\tilde{r} - \tilde{r}_s)} \right] \equiv -\tilde{\mathbf{V}}_0 w_{out}(\tilde{r}) \quad \text{for } \tilde{r} > \tilde{r}_s. \quad (4.15)$$

with

$$n = \frac{1}{2} \left(-1 + \sqrt{1 + 4\tilde{r}_v^2} \right). \quad (4.16)$$

This solution will be used as an input in the equation of motion (4.6).

4.2.3 Comparison with gravitational forces

To obtain an order of magnitude estimate of the strength of the LV effects, we compare the time dependent part of the LV force with the standard gravitational interactions, namely the gravitational force generated by the satellite halo itself and the tidal effects produced by the gravitational field of the host halo. From the equation (4.6) and using the results of the previous section it can be shown that the absolute value of the time dependent force produced by the LV coupling on a particle belonging to a satellite on circular orbit is

$$F_{\dot{u}} \simeq Y w(r) \frac{V_0^2}{R_0}, \quad (4.17)$$

where V_0 is the orbital velocity of the satellite in the host halo, R_0 is the distance from the center of the host and the function $w(r) \leq 1$ has been defined in (4.14), (4.15) and is shown for some cases in appendix A. The gravitational force generated by the satellite on a particle is given by

$$F_{sat} = \frac{GM(r)}{r^2} = V_c^2 \mathcal{M} \frac{r_s}{r^2}, \quad (4.18)$$

where $V_c^2 = GM_s/r_s$ and $\mathcal{M} = M(r)/M_s$. Hence,

$$\frac{F_{\dot{u}}}{F_{sat}} = Y w(r) \left(\frac{V_0}{V_c} \right)^2 \frac{M_s}{M(r)} \frac{r^2}{r_s R_0}. \quad (4.19)$$

Let us take typical values $V_0 \sim 200 \text{ km s}^{-1}$ and $V_c \sim 20 \text{ km s}^{-1}$, $r_s \sim 2 \text{ kpc}$ and $R_0 = 100 \text{ kpc}$. With these numbers the ratio between the two forces at $r = r_s$ is

$$\frac{F_{\dot{u}}}{F_{sat}} \sim 2 Y w(r_s). \quad (4.20)$$

The ranges of the LV parameters studied in this paper are listed in Table 1. We see that for these ranges of parameters there will be an extra force acting on the particles in the satellite comparable to the gravitational force. The effect is maximal at the edge of the satellite halo given that $|w(r)| \leq 1$ is a monotonically growing function, as can be see from figures 10 and 11 in the Appendix.

Let us also consider an order of magnitude estimate of the gravitational tidal force of the host halo. The force exerted by the host galaxy onto a particle that lies at the boundary of the satellite's halo (on the side facing the galactic center) is given by

$$F_{tidal} = \frac{GM_h}{(R_0 - r_s)^2} - \frac{GM_h}{R_0^2} \sim V_0^2 \frac{r_s}{R_0^2}, \quad (4.21)$$

where we have used the fact that $V_0 = \sqrt{GM_h/R_0}$. Hence, the ratio between the two forces is

$$\frac{F_{\dot{u}}}{F_{tidal}} = Y w(r_s) \frac{R_0}{r_s}. \quad (4.22)$$

Parameters values			
	Y	r_{sc} [kpc]	κ_A
Satellites:	0.05 – 0.95	1 – 35	10^{-13} – 10^{-9}
Cluster:	0.05 – 0.95	10 – 350	10^{-11} – 10^{-7}

Table 1. Range of the LV parameters explored. Y is the coupling strength between DM and the LV vector while r_{sc} is the screening scale radius. The third column is the corresponding range for the parameter κ_A . These tiny κ values are not constrained by any other observation.

If we insert characteristic values in the previous equation we find that at the edge of the satellite the force due to the LV vector can be ~ 100 times the tidal force. Furthermore, consider a satellite before it has undergone tidal stripping, so that its halo extends up to its original virial radius. In this case it turns out that the ratio between the two forces is $F_{\dot{u}}/F_{tidal} \sim 10Yw(r_v)$. This result has far reaching consequences as it shows that the LV force may provide a competing mechanism for halo disruption, in particular if the timescale for particle extraction due to the LV force is shorter than that of tidal stripping. This expectation is indeed confirmed by numerical simulations, see below.

4.3 Numerical results

In this section we present results from the numerical integration of equation (4.6) of a DM halo orbiting inside the halo of its host galaxy. We consider a system similar to the MW and two of its dwarf satellites, Draco and Fornax. This choice is particularly suited for our purposes. Draco is placed at a galactocentric distance of 82 kpc while Fornax is at 147 kpc. The motion of Fornax is compatible with a nearly circular orbit [40]. Draco motion is instead more controversial: observations from the *Hubble Space Telescope* placed it on a relatively circular orbit [35, 45], but more recent observations from *Subaru* telescope suggest an elliptical orbit [46]. Although this is an important aspect that must be taken into account in a more detailed study, it is not crucial for our analysis, so we assume a circular orbit for Draco as well. In order to make the investigation more complete and to explore a broader range of scales and velocities, we also consider the case of a test galaxy belonging to the Coma cluster. In Table 1 we show the ranges of parameters that these systems may be sensitive to. In particular, assuming a certain range for the values of the screening length r_{sc} and of Y determines through equation (4.5) the values of the LV parameter κ_A that one can explore. The range of parameters accessible to our study is well beyond those probed by other tests mentioned in section 2.

Table 2 lists the parameters of the halos that have been used in the numerical integration. For Draco we explore two scenarios with the same mass. Draco A: all the halo mass lies inside a radius of ~ 2 kpc which is the cutoff radius seen in the observations of the stellar component [39]. Draco B: the halo extends to a radius of ~ 20 kpc which corresponds to the virial radius of a halo with velocity dispersion of $\sim 10 \text{ km s}^{-1}$ consistent with the observations of Draco. These two scenarios may be seen as corresponding to satellites with and without gravitational

Parameters of Draco DM halo			
V_t	210 km s ⁻¹	tangential velocity of Draco satellite	[35]
σ_v	10 km s ⁻¹	velocity dispersion of Draco	[36, 37]
D	82 kpc	distance of Draco from the galactic center	[38]
T	2.2 Gyr	orbital period	
M_v	$6.2 \times 10^8 M_\odot$	Draco DM halo virial mass	
r_s	1.75 kpc	Draco actual DM halo radius [A]	[39]
r_s	17.5 kpc	Draco DM halo virial radius [B]	

Parameters of Fornax DM halo			
V_t	220 km s ⁻¹	tangential velocity of Fornax satellite	[40]
σ_v	10 km s ⁻¹	velocity dispersion of Fornax	[37, 41]
D	147 kpc	distance of Fornax from the galactic center	[38]
T	4.3 Gyr	orbital period	
M_v	$6.2 \times 10^8 M_\odot$	Fornax DM halo virial mass	
r_s	1.75 kpc	Fornax actual DM halo radius	[39]

Parameters of a DM galactic halo in Coma cluster			
V_t	1000 km s ⁻¹	tangential velocity of member galaxy	[42, 43]
σ_v	120 km s ⁻¹	velocity dispersion of galaxy DM particles	
D	2 Mpc	distance of the galaxy from the Coma center	
T	12 Gyr	orbital period	
M_v	$6.1 \times 10^{11} M_\odot$	galaxy virial mass	
r_s	175 kpc	galaxy DM halo virial radius	

Table 2. Halo parameters used in the integration of the equations of motion. See also [44] and references therein.

tidal stripping having occurred as they settle in their final orbit in the MW. In the case of Fornax the radius of the DM halo is the same as that of Draco A. The table also gives the parameters we adopt for the system of a galaxy in a cluster like Coma ($R_{\text{Coma}} \sim 3$ Mpc) [43]. In all cases the virial radii reported in table 2 are consistent with the observed one dimensional velocity dispersion.

The numerical solution is obtained by means of a 4(5) Runge–Kutta integration method over a Hubble time. We have considered both the gravitational potential and the LV force as external functions assuming that backreaction is negligible. This is a good approximations as long as departures from spherical symmetry are moderate.

To simulate the satellite halo, we have used 1500 particles with randomly oriented

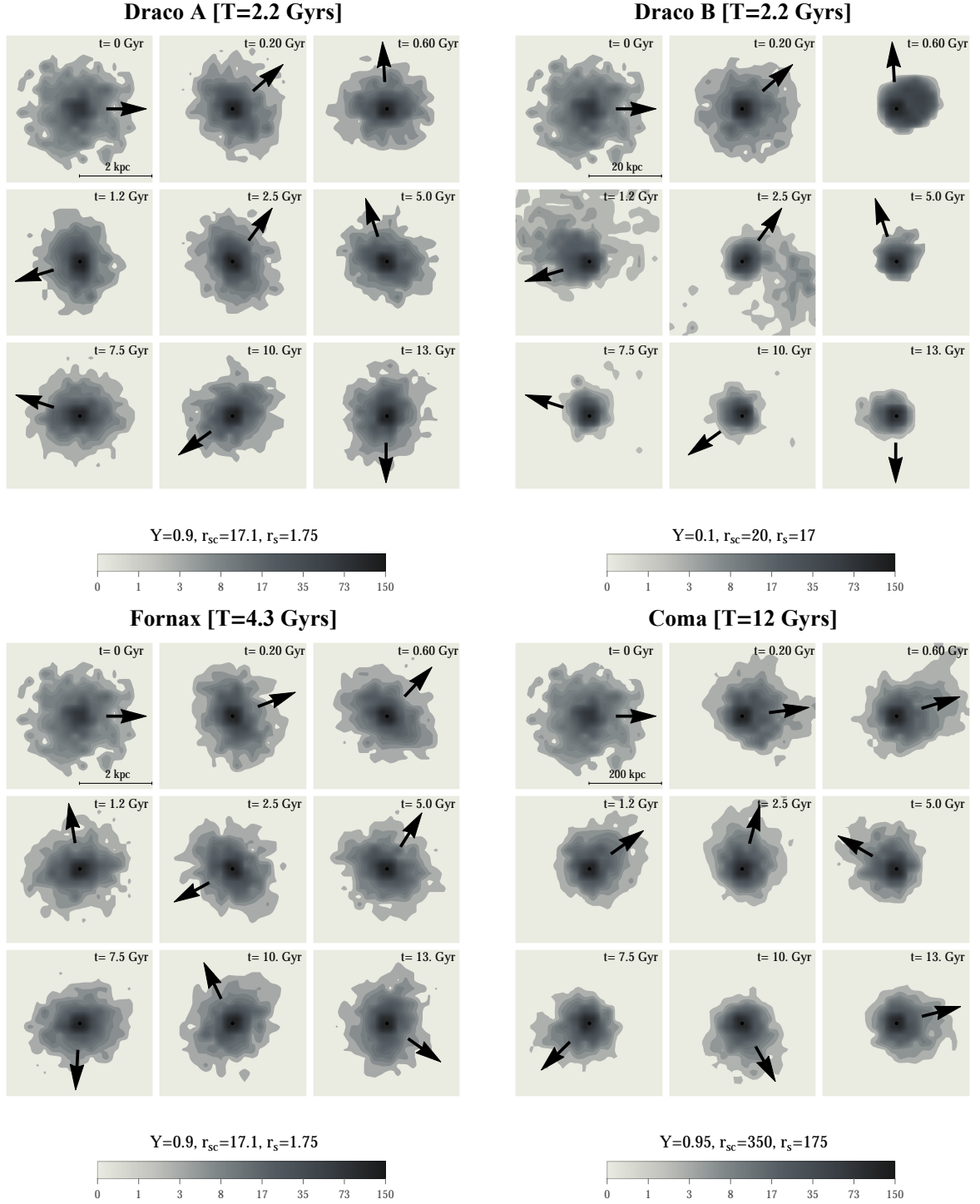


Figure 3. Particle distribution in the orbital plane of the satellite from the simulation output at different times. The 4 subplots correspond to the 4 considered systems with orbital periods T , as indicated in the figure. The top left panel in each subplot represents the initial configuration. The black arrow points towards the center of the host halo.

initial velocities. Their initial positions are adjusted in such a way that, under the influence of gravity alone, they would stay on circular orbits around the center of the satellite. The initial density distribution of particles follows an Einasto profile [47, 48] for which the mass enclosed inside a radius r is

$$M(r) = \left(1 - \frac{\Gamma(3n_E, (r/h)^{1/n_E})}{\Gamma(3n_E)}\right) \left(1 - \frac{\Gamma(3n_E, (r_s/h)^{1/n_E})}{\Gamma(3n_E)}\right)^{-1}, \quad (4.23)$$

where Γ is the incomplete gamma function, the mass is normalized such that $M(r = r_s) = 1$ and the parameter h satisfies $h = r_{-2}/(2n_E)^{n_E}$ where r_{-2} is the radius at which the slope $d \log \rho / d \log r = -2$. The slope parameter n_E decreases with halo mass and is $4.54 \lesssim n_E \lesssim 8.33$ [49], where the lower and higher values correspond to a cluster and a dwarf halo, respectively. In our simulation we adopt $n_E = 5.88$ and $r_{-2} = r_v/20$.

The LV force is provided by the potentials found in the previous section, namely equations (4.14) and (4.15). Notice that these have been derived assuming the particle distribution in the satellite follows an r^{-2} profile rather than an Einasto. However, in the situations we will consider, the deviations of the Einasto profile from the inverse square law are small and the two profiles are similar over the part of the satellite containing most of the mass.

4.3.1 Particle distribution

We begin with a general visual assessment of the particle distribution. This will serve as an introduction to the more quantitative analysis below.

Figure 3 shows the particle distribution in the plane of motion of the satellite at different times. The halo taken to be spherically symmetric at $t = 0$ is deformed at later times in a very specific way. The circular motion of the satellite produces a periodic LV force which turns the halo into elliptical shape with a time varying orientation. Another effect of the LV force is to enhance the particle distribution density at the center. Interestingly, a stable configuration is reached in all cases after 5 Gyr at the latest.

For Draco B the effect of LV force is particularly dramatic, as can be seen from figure 3 (top right). At the beginning we see a transient phase due to the fact that particles are initially placed on stable orbits according to gravity alone. Quickly after that the LV force kicks in and rapidly extracts particles from the outer shells, whereas the particle distribution in the central region gets tighter. We emphasize that this effect is purely due to the LV interaction, as the tidal gravitational force has been switched off in the simulations (see the discussion preceding equation (4.6)). Although this is a very extreme case, it is nonetheless instructive since it shows how the LV force may provide a very efficient mechanism for disrupting shallow sub-halos. This mechanism can operate on timescales shorter than the usual tidal disruption and, unlike the latter, gives rise to asymmetric tails of debris. A galactic halo in the Coma cluster exhibits similar: rapid mass extraction from the outer shell and then the halo settles to a stable configuration with a smaller radius, figure 3 (bottom right).

These examples demonstrate several interesting consequences of the LV force: it changes the density profile of the halo, it may remove a significant amount of particles and it changes the initially spherical distribution. In the next three subsections we will quantify these effects by analyzing the mass distribution inside the halos, the mass loss and the ellipticity of the halos as functions of the model parameters.

4.3.2 Radial mass profiles

We examine now how the mass distribution of the satellite halo is affected by the presence of the LV force. We compute the mass $M(r)$ within spherical shells from the particle distribution in the simulation. We select the simulation output at a sufficiently late time to ensure that the system has reached a steady state. In the normalization of $M(r)$ we include only particles inside the outer radius of the initial configuration.

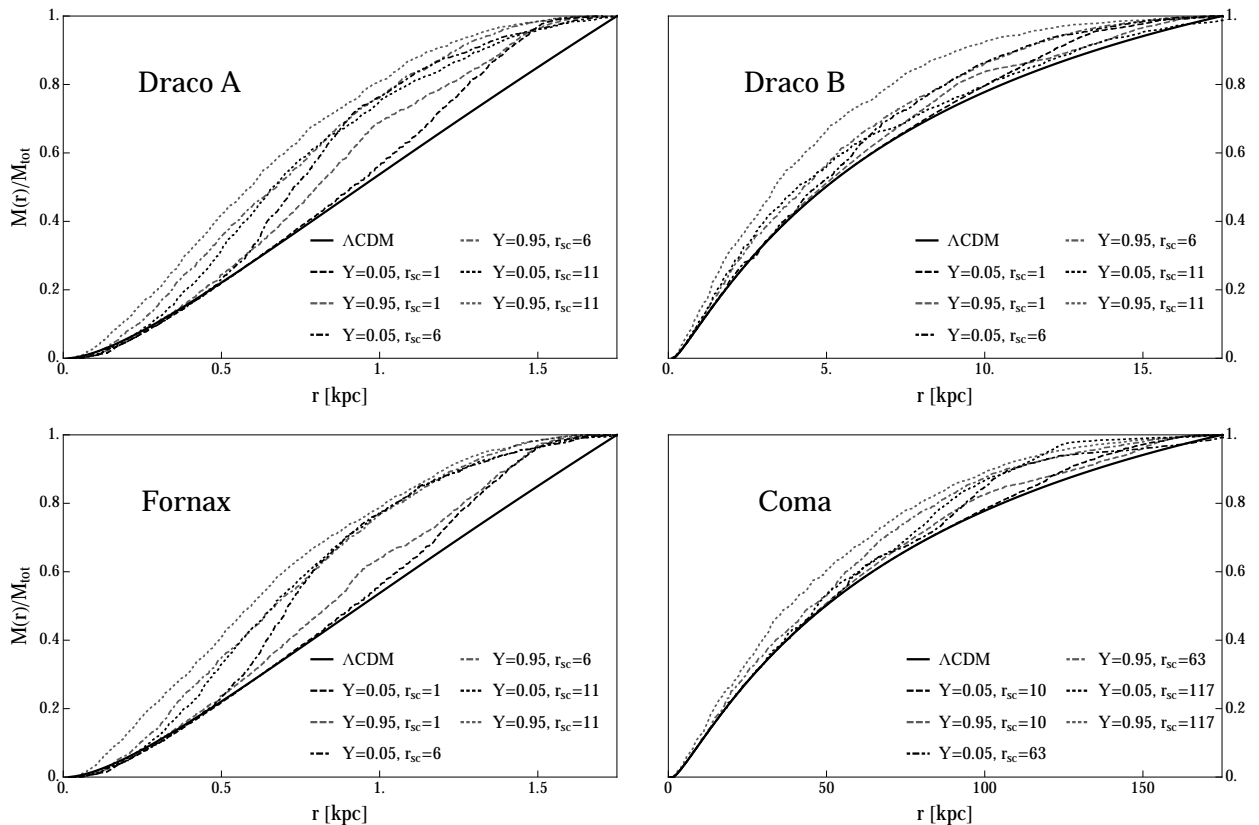


Figure 4. Mass within a given radius for Draco A (top left), Draco B (top right), Fornax (bottom left) and a galaxy in the Coma cluster (bottom right) for various values of r_{sc} and Y . The black line in each panel shows the initial distribution.

Curves of $M(r)$ are plotted in figure 4 for all systems. The solid line in each panel refers to the initial unperturbed profile. This profile would be maintained if the system were advanced according to gravity alone³. The other curves correspond to the particle distribution evolved with the LV force for several values of r_{sc} and Y , as indicated. The LV force introduces significant changes to the mass distribution of the subhalo. This confirms the visual assessment of Fig. 3: the evolved satellites are denser and more compact with respect to the solid line. For a quantitative assessment of the particle distribution we fit the evolved mass profile $M(r)$ by an Einasto functional form (cf. (4.23)) with both n_E and r_{-2} as free parameters. We find that, apart from the central regions, the Einasto profile provides a reasonable fit. However, the best fit values of n_E and r_{-2} deviate dramatically from the

³This is true also in the case of Draco B because we are neglecting the effects due to the tidal forces of the host halo.

observationally motivated range. For the values of r_{sc} and Y considered in the figure, the fit yields $0.61 \lesssim n_E \lesssim 1.62$ and $0.36 \lesssim r_{-2} \lesssim 0.71$ for Draco A, $2.4 \lesssim n_E \lesssim 4.94$ and $0.82 \lesssim r_{-2} \lesssim 2.02$ for Draco B, $0.61 \lesssim n_E \lesssim 1.9$ and $0.33 \lesssim r_{-2} \lesssim 0.71$ for Fornax and $2.35 \lesssim n_E \lesssim 4.41$ and $12.82 \lesssim r_{-2} \lesssim 20.83$ for a galaxy in Coma cluster.

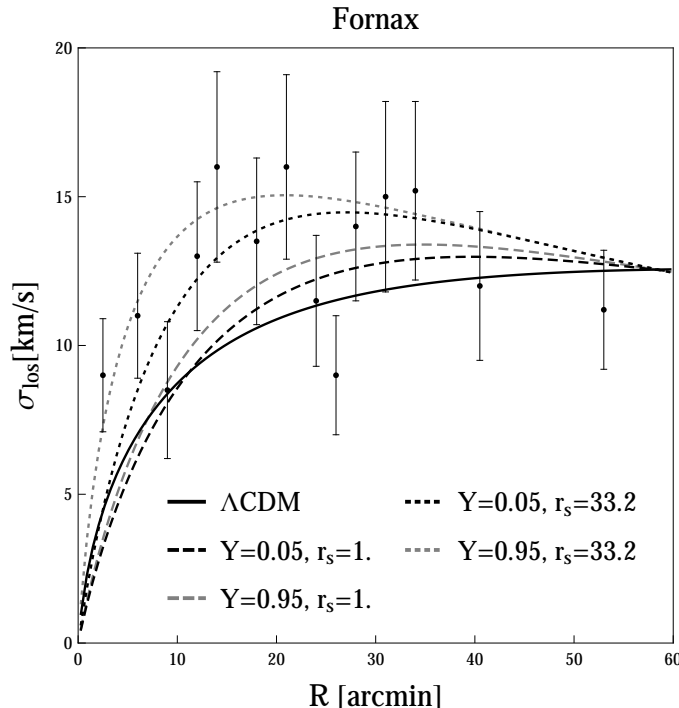


Figure 5. Theoretical predictions for the line-of-sight velocity dispersion compared with the observed values. The continuous line corresponds to σ_{los} obtained from an Einasto profile with $n_E = 5.88$ and $r_{-2} = r_v/20$ in Λ CDM model. The dashed and dotted lines correspond to different choices for the LV parameters. The data points and the 1σ error bars have been taken from [50].

Caution should be exercised in interpreting these results as they have been derived in a simplified model, which does not take into account the formation process of the satellite. It is nonetheless interesting to see if one can constrain the LV effect from observations of the stellar component. In particular, good measurements of the line-of-sight velocity dispersion of stars in Fornax are available [41, 50, 51]. Even if stars are not influenced by the LV force, their observed distribution and velocity dispersion are a probe of the underlying DM distribution through their gravitational interaction. Given the DM distribution in the simulation, one can thus predict the velocity dispersion of baryonic tracers (stars). Assuming circular orbits for the stars, we computed their line of sight velocity dispersion according to [52–54]

$$\sigma_{los}^2(R) = \frac{1}{I(R)} \int_R^\infty \left(\frac{R}{r}\right)^2 \frac{\nu(r)g(r)r^2}{\sqrt{r^2 - R^2}} dr, \quad (4.24)$$

where R is the projected distance from the subhalo center, $I(R)$ is the surface brightness [55, 56], and $\nu(r)$ is the 3D density of stars [57]. The gravitational acceleration $g(r)$ is due to the gravity of the DM in the simulation and a subdominant stellar component whose contribution is estimated using the observed stellar distribution in Fornax [58]. Figure 5 shows $\sigma_{los}(r)$ for $M(r)$ corresponding to the initial Einasto profile as well as evolved particle

distributions with several values of the LV parameters. The data shown in the figure do not allow to constrain the parameter space of the LV force. By looking at the plot one may be tempted to conclude that some of the LV curves fit the data better than the unperturbed one. However, to draw robust conclusions one should use more recent and precise data [59] which, in turn, require more precise simulations and a broader investigation of the relation between velocity dispersion and the underlying mass profile.

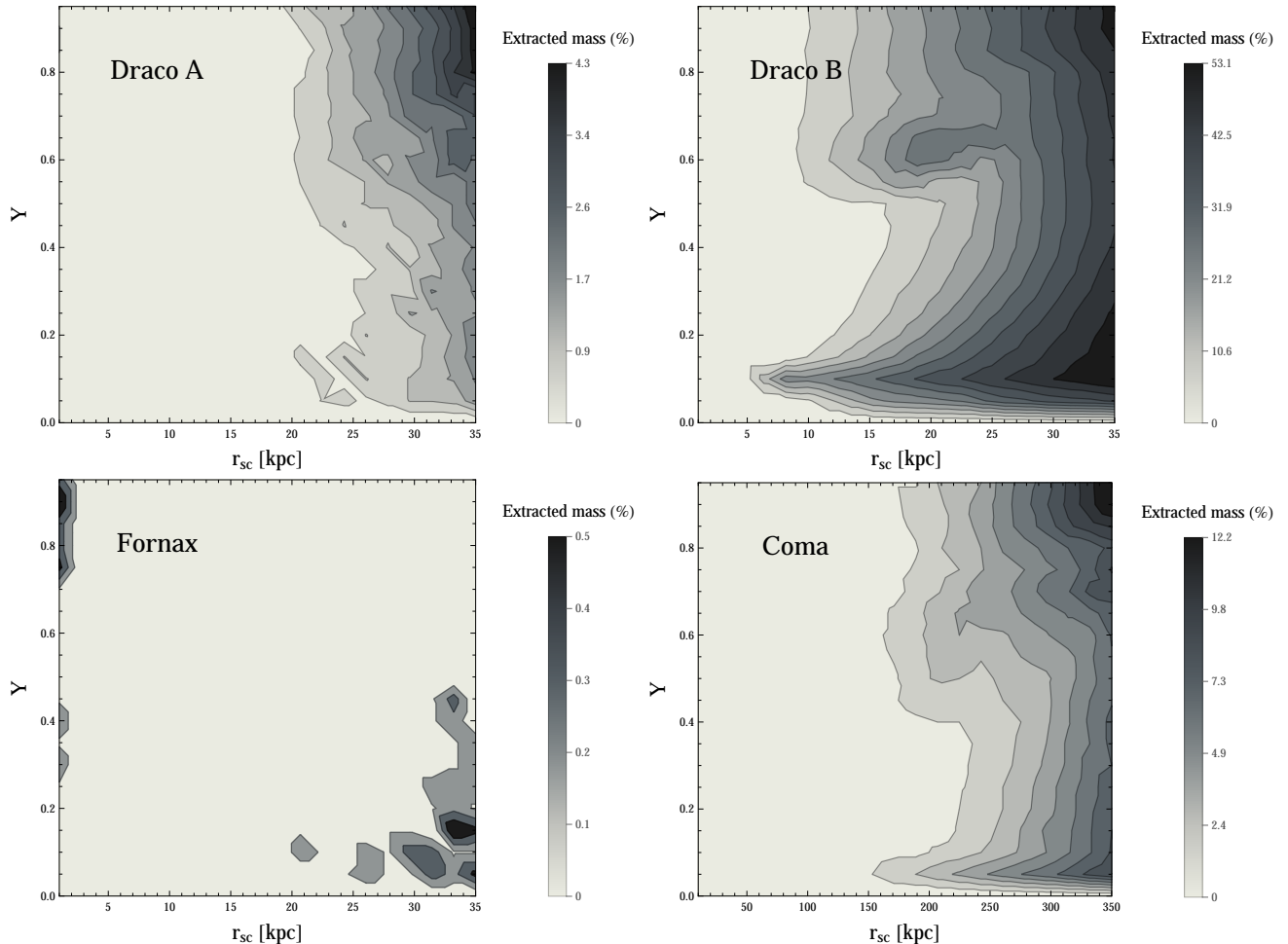


Figure 6. Extracted mass for the stripped Draco halo (top left), the unstripped Draco halo (top right), Fornax halo (bottom left) and a galaxy in the Coma cluster (bottom right) for various values of the parameters r_{sc} and Y .

4.3.3 Mass extraction

We now quantify the mass extracted from the halo by the LV force as the mass that lies outside the initial radius of the object at a given time⁴. Figures 6 plot the mass loss after a Hubble time as a function of the parameters r_{sc} and Y . As can be seen from the plots, for the most compact satellites the mass loss is small, almost non existing in the case of Fornax. However, it is very pronounced for extended subhalos, reaching a peak of 50% in Draco B.

⁴Notice that this does not imply that all particles carrying this mass are not bound to the object anymore. However, we have checked that there is no significant change in the enclosed mass after a few time steps.

This last case is particularly interesting because most of the mass is extracted during the first orbit, cf. Fig. 3. In comparison, the amount of mass extracted by tidal stripping is as high as 60% of the initial mass after the first pericentric passage [60]. In general, the typical timescale of mass extraction by the LV force will depend on the particular set of parameters but we found that in many cases it is shorter than the one associated to tidal effects. Another interesting effect is the dependence on the distance from the center of the host galaxy. Even if Draco A and Fornax have a similar initial configuration, the former experiences a larger mass loss since it is closer to the center of the MW.

4.3.4 Ellipticity

In 4.3.1 we have mentioned deviations from a spherical shape as another observable signature of LV. In order to assess these deviations quantitatively, we have computed the ellipticity parameters from the particle distribution in the simulation output. We define a coordinate system (x, y, z) with origin centered at and comoving with the core of the satellite. The directions of the 3 axes are fixed with respect to the host halo. Furthermore, the xy plane is defined by the orbital motion of the satellite inside the host halo.

The ellipticity is characterized by the quadratic moments of the density distribution,

$$Q_{ij} = \frac{1}{N} \sum_{p=1}^N x_p^i x_p^j, \quad (4.25)$$

where the summation is over all N particles of the subhalo. We define the ellipticity parameters in the plane (x, y) as

$$(\epsilon_1, \epsilon_2) = \left(\frac{Q_{xx} - Q_{yy}}{Q_{xx} + Q_{yy} + 2(Q_{xx}Q_{yy} - Q_{xy}^2)^{1/2}}, \frac{2Q_{xy}}{Q_{xx} + Q_{yy} + 2(Q_{xx}Q_{yy} - Q_{xy}^2)^{1/2}} \right), \quad (4.26)$$

and similarly for the plane (x, z) . Denoting the major and minor axes by a and b respectively, the ellipticity parameters can be written as

$$\epsilon_1 = \frac{1 - q}{1 + q} \cos(2\theta), \quad (4.27)$$

$$\epsilon_2 = \frac{1 - q}{1 + q} \sin(2\theta), \quad (4.28)$$

where $q = b/a$, and θ is the angle between the major axis and the x -direction.

We have computed the ellipticity parameters for Fornax and Draco for $Y = 0.95$, $r_{sc} = 11.7$ kpc and $Y = 0.5$, $r_{sc} = 8.2$ kpc. In figure 7 we plot the time evolution of q in the orbital plane of the satellite. The irregularities in the curves are due to the discreteness of the particle distribution. The light gray curve in the plots corresponds to no LV force i.e. $q = 1$. The other curves reach values substantially different from unity, almost immediately after the force is switched on and stay constant over a whole Hubble time.

On the other hand, the ellipticity parameter q in the orthogonal plane (x, z) exhibits pronounced oscillations at approximately half the orbital period, see Fig. 8. Recall that the plane (x, z) is fixed with respect to the host halo. Then the dependences shown in Figs. 7, 8 imply that the satellite has a prolate ellipsoidal shape with the major axis lying in the orbital plane and sustaining an almost constant angle with the direction of motion.

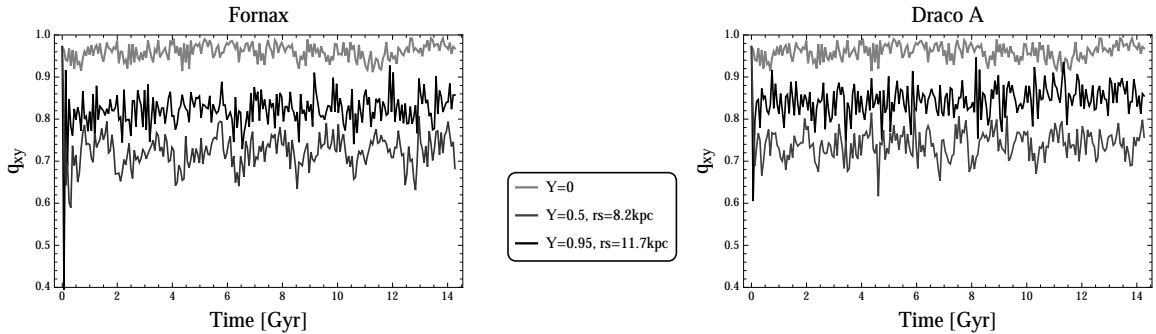


Figure 7. Time evolution of $q = b/a$ parallel to the orbital plane for three sets of values of the parameters (Y, r_{sc}) : $(0, -)$ light gray, $(0.5, 8.2 \text{ kpc})$ dark gray and $(0.95, 11.7 \text{ kpc})$ black line for Fornax (left) and Draco A (right).

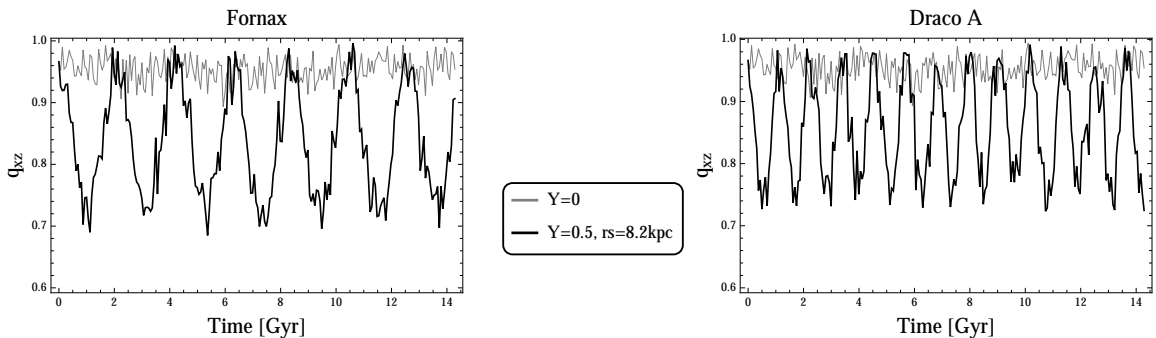


Figure 8. Time evolution of $q = b/a$ in the plane orthogonal to the orbital motion for two sets of values of the parameters (Y, r_{sc}) : $(0, -)$ light gray, $(0.5, 8.2 \text{ kpc})$ black line for Fornax (left) and Draco A (right).

The values of ellipticity obtained in our simulations are compatible with observations [61, 62]. Nevertheless they can be also explained within pure Λ CDM [63, 64]. A more refined analysis is needed in order to tell whether the ellipticity generated by the LV force exceeds the one produced by gravitational forces alone.

It is interesting to further examine the orientation of the major axis with respect to the direction of motion of the satellite. To address this point we show in Fig. 9 the angle between the major axis of Draco A and the direction to the center of the host halo (this direction is perpendicular to the velocity of the satellite). As advocated above, the angle changes only slightly during the orbital period. However, it precesses significantly on longer timescales comparable to the Hubble time. Using the expressions (4.14), (4.15) for the LV vector one finds that the LV force acting on a particle in the subhalo (the term in square brackets in equation (4.6)) contains a contribution

$$Y w'(\tilde{r}) [(\tilde{\mathbf{v}}_p \cdot \hat{\mathbf{r}}) \tilde{V}_0^i - (\tilde{\mathbf{v}}_p \cdot \tilde{\mathbf{V}}_0) \hat{r}^i],$$

where \hat{r}^i is the unit vector pointing from the center of the satellite to the particle's position. By switching of and on this term in numerical simulations we have identified it as being responsible for the secular change in the subhalo orientation shown in Fig. 9.

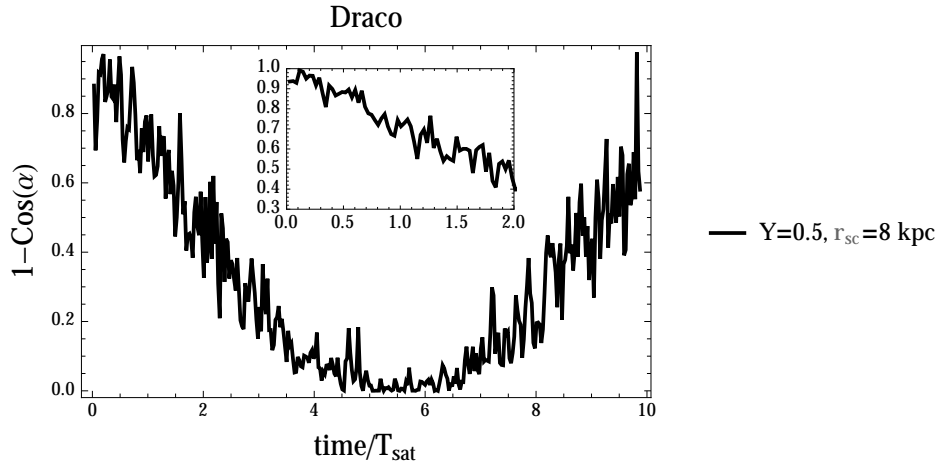


Figure 9. Time evolution of the angle between the ellipticity vector and the one pointing towards the center of the host halo for Draco as a function of time measured in revolution periods ($T_{Draco} = 2.17$ Gyrs). The LV parameters are $Y = 0.5$ and $r_{sc} = 8$ kpc. Unity corresponds to orthogonality while zero means alignment between the two vectors.

5 Discussion and conclusions

We have performed a preliminary investigation of the dynamics of galactic satellites in the presence of a LV force in the DM sector. This extends previous studies of the effects of LV in DM to shorter scales. This is a promising arena for testing LV in the dark sector with potential observational signatures. The relevant range of parameters enters through the screening scale r_{sc} (4.5) and direct effects related to the DM coupling to LV, Y . The typical probed range $r_{sc} \sim \text{kpc}$ is remarkably different from that constrained from linear dynamics at large scales, $r_{sc} \sim \text{Mpc}$. The price to pay is the complexity of modeling the highly non linear structures whose detailed dynamical evolution must ultimately be followed with full numerical simulations. The goal of the present paper has been to identify generic signatures of LV forces. Hence, we have opted to follow a simplified scheme designed to capture the main consequences of the model. Our focus have been the dynamics of a satellite orbiting around its host halo. For this reason we have been concerned only with the effects on the satellite alone. Therefore, we have restricted the analysis to the parameter regime for which the LV effects of the host halo are screened. Besides, we neglected tidal gravitational forces and left out the formation process of the satellite – host halo system.

We have identified several interesting effects which could have substantial implications on the evolution of satellite galaxies: An enhancement of the inner halo density accompanied with mass extraction from the outer regions and a distortion of the halo shape. The main features of these effects are:

Mass profile: The LV force produces a significant compression of the satellite halo. This translates into a different gravitational field with respect to the Λ CDM model acting on the stellar component. In this respect, a potential way to seek signatures of (or constraints on) LV is by measurements of the velocity dispersion profile of the stars in the satellite as we have discussed in section 4.3.2. We have found that the curves obtained within LV models differ significantly from those where no LV force is acting. However, both are still compatible with the observations cf. Fig. 5. It would be interesting to explore if more precise data [59] are

capable to discriminate between Lorentz invariant and LV models, which, however, requires more detailed and realistic numerical simulations.

Total mass of subhalos: A feature of the LV force is its ability to efficiently extract matter from the outskirts of subhalos. This mechanism for particle extraction works in addition to tidal stripping by the gravitational force field of the host halo. Depending on the relative importance of the two effects, various scenarios can be envisaged. If the gravitational tidal stripping is very efficient, we should not expect much particle extraction via LV, as we have seen in the case of Draco A and Fornax. However, if the opposite situation is realized, as is the case for Draco B, the LV yanks matter at the outer halo regions and acts on shorter timescales than the gravitational tidal stripping, leaving the latter largely irrelevant. This could result in a different equilibrium configuration. Although the residual mass from the two processes is similar, the final halo will show very different characteristics that will allow for a distinction between the two mechanisms. Tidal stripping does not greatly alter the density profile, in contrast to the LV force. Moreover, gravitational stripping produces symmetric streams (leading and trailing); in the case of LV force, streams of extracted stars would be asymmetric, reflecting the preferred direction defined by the vector. This latter feature can be noticed in the right panels of figure 3 where a characteristic tail is formed after a significant amount of mass has been extracted from the satellite and more dramatically in the second figure of the Draco B case.

Ellipticity of the satellite halo: The LV force produces a distortion in the shape of subhalos. We found that the ellipticity of the altered shapes is in the ballpark of the values observed for dwarf satellites in the Local Group [61, 62], but the latter are also compatible with pure Λ CDM simulations [63, 64]. More detailed numerical studies are required to tell apart the LV effect from the purely gravitational one. The distortion alters the gravitational potential felt by stars, which can be directly probed by measurements of the stellar velocity dispersion. Unfortunately, inferring the shape-related LV signatures is hampered by the precession of the major axis which smears the correlation of LV generated ellipticity with the direction of motion of the satellite.

The challenge in constraining LV effects is that standard gravity could also be associated with similar phenomenology. Our analysis points out several interesting features and motivates a more sophisticated numerical and observational modeling for disentangling LV from purely gravitational signatures.

As we discussed in the introduction, there is a strong motivation to test Lorentz invariance. For low energies and late time Universe this requires the study of models with Lorentz violating fields. These fields are generically coupled to the other ‘standard’ components of the Universe, and these interactions control the effects of LV in different observations. Although the couplings to the standard model particles are highly constrained, the same is not true for DM. Given the current and forthcoming observational data, the investigation of the effects of LV in DM models using small scales structures may not only reveal interesting aspects of how such structures have formed but could also shed light on this fundamental aspects of Nature.

Acknowledgments

This research was supported by the I-CORE Program of the Planning and Budgeting Committee, THE ISRAEL SCIENCE FOUNDATION (grants No. 1829/12 and No. 203/09), the Asher Space Research Institute. D. Bettoni acknowledges financial support from “Fondazione Angelo Della Riccia” and from the SFB-Transregio TRR33 “The Dark Universe”. D. Bettoni wish to thank Nordita where a large part of this work has been carried on. D. Blas would like to thank the Physics Department of the Universidad de Chile for its warm hospitality during the completion of this work. The work of S.S. is supported by the Swiss National Science Foundation.

A analytic solution for the LV vector

We give now the detailed derivation of the solutions of the equation for the LV vector \mathbf{u} discussed in section 4.2. Here, we consider the general case of a spherical object (the satellite) which has a core of constant density surrounded by a shell where the density is dropping as r^{-2} and whose particles are collectively moving with the speed \mathbf{V}_s . The satellite moves inside a bigger object (the host halo) with constant density and whose particles are moving with constant bulk velocity \mathbf{V}_h . We have to solve the following three equations

$$\tilde{\Delta}\tilde{u}^i = \alpha_c^2 (\tilde{u}^i - \tilde{V}_s^i), \quad \text{if } r \leq r_c, \quad (\text{A.1})$$

$$\tilde{\Delta}\tilde{u}^i = \left(\frac{\tilde{r}_v}{\tilde{r}}\right)^2 (\tilde{u}^i - \tilde{V}_s^i), \quad \text{if } r_c \leq r \leq r_s, \quad (\text{A.2})$$

$$\tilde{\Delta}\tilde{u}^i = \alpha_h^2 (\tilde{u}^i - \tilde{V}_h^i), \quad \text{if } r \geq r_s, \quad (\text{A.3})$$

where r_v and r_s are the virial and the actual radius of the satellite respectively and r_c is the radius of the core. The scale r_{sc} is defined in (4.5). Requiring that the transition between the three regions is smooth, i.e. $\rho_a(\tilde{r}_a) = \rho_s(\tilde{r}_a)$ for $a = h, c$, yields $\alpha_a = \tilde{r}_v/\tilde{r}_a$. The solution to these equations reads,

$$\tilde{u}_c^i(\tilde{r}) = \tilde{V}_s^i + C_1^i \frac{e^{-\alpha_c \tilde{r}}}{\tilde{r}} + C_2^i \frac{e^{\alpha_c \tilde{r}}}{\tilde{r}}, \quad \text{if } r \leq r_c, \quad (\text{A.4})$$

$$\tilde{u}_s^i(\tilde{r}) = \tilde{V}_s^i + C_3^i \tilde{r}^{n_-} + C_4^i \tilde{r}^{n_+}, \quad \text{if } r_c \leq r \leq r_s, \quad (\text{A.5})$$

$$\tilde{u}_h^i(\tilde{r}) = \tilde{V}_h^i + C_5^i \frac{e^{-\alpha_h \tilde{r}}}{\tilde{r}} + C_6^i \frac{e^{\alpha_h \tilde{r}}}{\tilde{r}}, \quad \text{if } r \geq r_s, \quad (\text{A.6})$$

where $n_+ = (-1 + \sqrt{1 + 4\tilde{r}_v^2})/2$ and $n_- = (-1 - \sqrt{1 + 4\tilde{r}_v^2})/2$.

The solutions are required to be finite at $r = 0$ and vanishing at infinite radius. This fixes two of the six integration constants. In particular, we get $C_1 = -C_2$ and $C_6 = 0$. By matching the solutions at $r = r_c$ and at $r = r_s$ we obtain

$$\tilde{u}_c^i(\tilde{r}) = \tilde{V}_s^i - \left(\tilde{V}_s^i - \tilde{V}_h^i\right) \frac{\tilde{r}_c^{n_+} - \Gamma_c \tilde{r}_c^{n_-}}{\tilde{r}_s^{n_+} \kappa_+ - \tilde{r}_s^{n_-} \kappa_- \Gamma_c} \frac{\sinh(\alpha_c \tilde{r})}{\sinh(\alpha_c \tilde{r}_c)} \frac{\tilde{r}_c}{\tilde{r}}, \quad \text{if } r \leq r_c, \quad (\text{A.7})$$

$$\tilde{u}_s^i(r) = \tilde{V}_s^i - \left(\tilde{V}_s^i - \tilde{V}_h^i\right) \frac{\tilde{r}^{n_+} - \Gamma_c \tilde{r}^{n_-}}{\tilde{r}_s^{n_+} \kappa_+ - \tilde{r}_s^{n_-} \kappa_- \Gamma_c}, \quad \text{if } r_c \leq r \leq r_s, \quad (\text{A.8})$$

$$\tilde{u}_h^i(r) = \tilde{V}_h^i + \left(\tilde{V}_s^i - \tilde{V}_h^i\right) \left[1 - \frac{\tilde{r}_s^{n_+} - \Gamma_c \tilde{r}_s^{n_-}}{\tilde{r}_s^{n_+} \kappa_+ - \tilde{r}_s^{n_-} \kappa_- \Gamma_c}\right] \frac{e^{-\alpha_h(\tilde{r}-\tilde{r}_s)}}{\tilde{r}/\tilde{r}_s}, \quad \text{if } r \geq r_s, \quad (\text{A.9})$$

where

$$\kappa_{\pm} = 1 + \frac{n_{\pm}}{1 + \alpha_h \tilde{r}_s}, \quad \Gamma_c = \frac{\gamma_c - n_+}{\gamma_c - n_-} \cdot \frac{\tilde{r}_c^{n_+}}{\tilde{r}_c^{n_-}}, \quad \gamma_c = \alpha_c \tilde{r}_c \coth(\alpha_c \tilde{r}_c) - 1. \quad (\text{A.10})$$

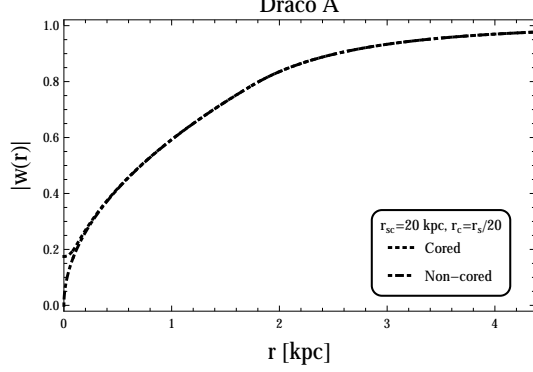


Figure 10. Comparison between the analytic solutions for the LV vector u^i obtained with a pure $\rho \sim r^{-2}$ profile and with a $\rho \sim r^{-2}$ profile that has a core of constant density, in the case of Draco A. Plotted is the radial time independent part of the LV solution, $|w|$, defined in (4.14) and (4.15). The screening scale is $r_{sc} = 20$ kpc and the virial radius is $r_v = 20$ kpc.

From this general solution we can recover the two limits that we have used in this work, namely the inverse square law and the purely constant profiles. To get the first one we take $r_c = 0$. In this case the solution is

$$\tilde{u}_s^i(\tilde{r}) = \tilde{V}_s^i + \left(\tilde{V}_h^i - \tilde{V}_s^i \right) \frac{1}{1 + \frac{n_+}{\alpha_h \tilde{r}_s + 1}} \left(\frac{\tilde{r}}{\tilde{r}_s} \right)^{n_+} \quad (\text{A.11})$$

$$\tilde{u}_h^i(\tilde{r}) = \tilde{V}_h^i - \left(\tilde{V}_h^i - \tilde{V}_s^i \right) \frac{n_+}{1 + n_+ + \alpha_h \tilde{r}_s} \frac{e^{-\alpha_h(\tilde{r} - \tilde{r}_s)}}{\tilde{r}/\tilde{r}_s}. \quad (\text{A.12})$$

The second limit is obtained by $r_c \rightarrow r_s$ and defining $\alpha = \alpha_h/\alpha_c$, yielding the solution

$$\tilde{u}_s^i(\tilde{r}) = \tilde{V}_s^i + \left(\tilde{V}_h^i - \tilde{V}_s^i \right) \left[\tilde{r}_s + \frac{\alpha_c^{-1} \sinh(\alpha_c \tilde{r}_c) - \tilde{r}_c \cosh(\alpha_c \tilde{r}_c)}{\alpha \sinh(\alpha_c \tilde{r}_c) + \cosh(\alpha_c \tilde{r}_c)} \right] \frac{\sinh(\alpha_c \tilde{r})}{\sinh(\alpha_c \tilde{r}_c)} \frac{1}{\tilde{r}} \quad (\text{A.13})$$

$$\tilde{u}_h^i(\tilde{r}) = \tilde{V}_h^i + \left(\tilde{V}_h^i - \tilde{V}_s^i \right) \frac{\alpha_c^{-1} \sinh(\alpha_c \tilde{r}_c) - \tilde{r}_c \cosh(\alpha_c \tilde{r}_c)}{\alpha \sinh(\alpha_c \tilde{r}_c) + \cosh(\alpha_c \tilde{r}_c)} \frac{e^{-\alpha_h(\tilde{r} - \tilde{r}_s)}}{\tilde{r}}. \quad (\text{A.14})$$

In figures 10 and 11 we show solutions for $\omega(r)$ (as defined in (4.14) and (4.15)) obtained from an inverse square law matter distribution for Draco A with and without a core for $r_{sc} = 20$ and $r_{sc} = 2$ respectively. In the first case there is a slight difference between the two curves in the center of the satellite, whereas in the second case the curves coincide. In both cases the LV force acting on particles inside the core is suppressed. This last point is exploited in the definition of the satellite reference frame used for the numerical formulation of the problem. In fact, we can consider this inner region as screened and consequently following the standard Newtonian motion. This in turns defines the reference frame in which the dynamics of particles in the subhalo is governed by the equation (4.6). In the second case $r_{sc} \leq r_s$ and the LV vector solution is constant almost up to the edge of the satellite as can be seen in figure 11. This is a consequence of the screening mechanism characteristic of the LV model.

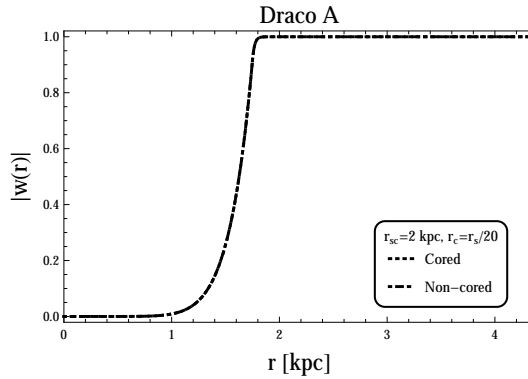


Figure 11. Same as Fig. 10, but for $r_{sc} = 2$ kpc and the virial radius is $r_v = 20$ kpc. In this case the two curves coincide.

References

- [1] PLANCK collaboration, P. A. R. Ade et al., *Planck 2015 results. XIII. Cosmological parameters*, [1502.01589](#).
- [2] C. M. Will, *The Confrontation between General Relativity and Experiment*, *Living Rev. Rel.* **17** (2014) 4, [[1403.7377](#)].
- [3] D. Mattingly, *Modern tests of Lorentz invariance*, *Living Rev. Rel.* **8** (2005) 5, [[gr-qc/0502097](#)].
- [4] V. A. Kostelecky and N. Russell, *Data Tables for Lorentz and CPT Violation*, *Rev. Mod. Phys.* **83** (2011) 11–31, [[0801.0287](#)].
- [5] S. Liberati and D. Mattingly, *Lorentz breaking effective field theory models for matter and gravity: theory and observational constraints*, [1208.1071](#).
- [6] S. Liberati, *Tests of Lorentz invariance: a 2013 update*, *Class. Quant. Grav.* **30** (2013) 133001, [[1304.5795](#)].
- [7] E. Berti et al., *Testing General Relativity with Present and Future Astrophysical Observations*, *Class. Quant. Grav.* **32** (2015) 243001, [[1501.07274](#)].
- [8] V. A. Kostelecky and S. Samuel, *Spontaneous Breaking of Lorentz Symmetry in String Theory*, *Phys. Rev.* **D39** (1989) 683.
- [9] N. E. Mavromatos, *Lorentz Invariance Violation from String Theory*, *PoS QG-PH* (2007) 027, [[0708.2250](#)].
- [10] P. Horava, *Quantum Gravity at a Lifshitz Point*, *Phys. Rev.* **D79** (2009) 084008, [[0901.3775](#)].
- [11] D. Blas, O. Pujolas and S. Sibiryakov, *On the Extra Mode and Inconsistency of Horava Gravity*, *JHEP* **10** (2009) 029, [[0906.3046](#)].
- [12] D. Blas and S. Sibiryakov, *Technically natural dark energy from Lorentz breaking*, *JCAP* **1107** (2011) 026, [[1104.3579](#)].
- [13] B. Audren, D. Blas, J. Lesgourgues and S. Sibiryakov, *Cosmological constraints on Lorentz violating dark energy*, *JCAP* **1308** (2013) 039, [[1305.0009](#)].
- [14] N. Arkani-Hamed, P. Creminelli, S. Mukohyama and M. Zaldarriaga, *Ghost inflation*, *JCAP* **0404** (2004) 001, [[hep-th/0312100](#)].
- [15] M. M. Ivanov and S. Sibiryakov, *UV-extending Ghost Inflation*, *JCAP* **1405** (2014) 045, [[1402.4964](#)].

- [16] P. Adshead, D. Blas, C. P. Burgess, P. Hayman and S. P. Patil, *Magnon Inflation: Slow Roll with Steep Potentials*, *JCAP* **1611** (2016) 009, [[1604.06048](#)].
- [17] T. Jacobson and D. Mattingly, *Gravity with a dynamical preferred frame*, *Phys. Rev.* **D64** (2001) 024028, [[gr-qc/0007031](#)].
- [18] D. Blas, O. Pujolas and S. Sibiryakov, *Models of non-relativistic quantum gravity: The Good, the bad and the healthy*, *JHEP* **04** (2011) 018, [[1007.3503](#)].
- [19] T. Jacobson, S. Liberati and D. Mattingly, *Lorentz violation at high energy: Concepts, phenomena and astrophysical constraints*, *Annals Phys.* **321** (2006) 150–196, [[astro-ph/0505267](#)].
- [20] L. Shao, R. N. Caballero, M. Kramer, N. Wex, D. J. Champion and A. Jessner, *A new limit on local Lorentz invariance violation of gravity from solitary pulsars*, *Class. Quant. Grav.* **30** (2013) 165019, [[1307.2552](#)].
- [21] K. Yagi, D. Blas, E. Barausse and N. Yunes, *Constraints on Einstein-ether theory and Hoava gravity from binary pulsar observations*, *Phys. Rev.* **D89** (2014) 084067, [[1311.7144](#)].
- [22] D. Blas and E. Lim, *Phenomenology of theories of gravity without Lorentz invariance: the preferred frame case*, *Int. J. Mod. Phys.* **D23** (2015) 1443009, [[1412.4828](#)].
- [23] D. Colladay and V. A. Kostelecky, *Lorentz violating extension of the standard model*, *Phys. Rev.* **D58** (1998) 116002, [[hep-ph/9809521](#)].
- [24] D. Blas, M. M. Ivanov and S. Sibiryakov, *Testing Lorentz invariance of dark matter*, *JCAP* **1210** (2012) 057, [[1209.0464](#)].
- [25] B. Audren, D. Blas, M. M. Ivanov, J. Lesgourgues and S. Sibiryakov, *Cosmological constraints on deviations from Lorentz invariance in gravity and dark matter*, *JCAP* **1503** (2015) 016, [[1410.6514](#)].
- [26] J. A. Frieman and B. A. Gradwohl, *Dark matter and the equivalence principle*, *Science* **260** (1993) 1441–1442.
- [27] M. Kesden and M. Kamionkowski, *Galilean Equivalence for Galactic Dark Matter*, *Phys. Rev. Lett.* **97** (2006) 131303, [[astro-ph/0606566](#)].
- [28] J. A. Keselman, A. Nusser and P. J. E. Peebles, *Cosmology with Equivalence Principle Breaking in the Dark Sector*, *Phys. Rev.* **D81** (2010) 063521, [[0912.4177](#)].
- [29] N. Mohapi, A. Hees and J. Larena, *Test of the Equivalence Principle in the Dark Sector on Galactic Scales*, *JCAP* **1603** (2016) 032, [[1510.06198](#)].
- [30] T. Jacobson, *Einstein-aether gravity: A Status report*, *PoS QG-PH* (2007) 020, [[0801.1547](#)].
- [31] B. Z. Foster and T. Jacobson, *Post-Newtonian parameters and constraints on Einstein-aether theory*, *Phys. Rev.* **D73** (2006) 064015, [[gr-qc/0509083](#)].
- [32] S. M. Carroll and E. A. Lim, *Lorentz-violating vector fields slow the universe down*, *Phys. Rev.* **D70** (2004) 123525, [[hep-th/0407149](#)].
- [33] A. Marakulin and S. Sibiryakov, *Linearized supergravity with a dynamical preferred frame*, 2016.
- [34] W. Dehnen, D. McLaughlin and J. Sachania, *The velocity dispersion and mass profile of the milky way*, *Mon. Not. Roy. Astron. Soc.* **369** (2006) 1688–1692, [[astro-ph/0603825](#)].
- [35] C. Pryor, S. Piatek and E. W. Olszewski, *Proper Motion of the Draco Dwarf Galaxy Based On Hubble Space Telescope Imaging*, *Astron. J.* **149** (2015) 42, [[1407.3509](#)].
- [36] R. R. Munoz, P. M. Frinchaboy, S. R. Majewski, J. R. Kuhn, M.-Y. Chou, C. Palma et al., *Exploring halo substructure with giant stars. 8. The Velocity dispersion profiles of the Ursa Minor and Draco dwarf spheroidals at large angular separations*, *Astrophys. J.* **631** (2005) L137–L142, [[astro-ph/0504035](#)].

- [37] M. G. Walker, M. Mateo, E. W. Olszewski, O. Y. Gnedin, X. Wang, B. Sen et al., *Velocity Dispersion Profiles of Seven Dwarf Spheroidal Galaxies*, *Astrophys. J.* **667** (2007) L53, [[0708.0010](#)].
- [38] M. Mateo, *Dwarf galaxies of the Local Group*, *Ann. Rev. Astron. Astrophys.* **36** (1998) 435–506, [[astro-ph/9810070](#)].
- [39] B. Moore, C. Calcaneo-Roldan, J. Stadel, T. R. Quinn, G. Lake, S. Ghigna et al., *Dark matter in Draco and the local group: implications for direct detection experiments*, *Phys. Rev.* **D64** (2001) 063508, [[astro-ph/0106271](#)].
- [40] S. Piatek, C. Pryor, E. W. Olszewski, H. C. Harris, M. Mateo, D. Minniti et al., *Proper motions of dwarf spheroidal galaxies from Hubble Space Telescope imaging. 1. Method and a preliminary measurement for Fornax*, *Astron. J.* **124** (2002) 3198, [[astro-ph/0209430](#)].
- [41] M. G. Walker, M. Mateo, E. W. Olszewski, R. A. Bernstein, X. Wang and M. Woodroffe, *Internal kinematics of the Fornax dwarf spheroidal galaxy*, *Astron. J.* **131** (2006) 2114–2139, [[astro-ph/0511465](#)].
- [42] M. F. Struble and H. J. Rood, *A compilation of redshifts and velocity dispersions for aco clusters*, *The Astrophysical Journal Supplement Series* **125** (1999) 35.
- [43] E. L. Lokas and G. A. Mamon, *Dark matter distribution in the Coma cluster from galaxy kinematics: Breaking the mass - anisotropy degeneracy*, *Mon. Not. Roy. Astron. Soc.* **343** (2003) 401, [[astro-ph/0302461](#)].
- [44] A. W. McConnachie, *The observed properties of dwarf galaxies in and around the Local Group*, *Astron. J.* **144** (2012) 4, [[1204.1562](#)].
- [45] M. S. Pawlowski and P. Kroupa, *The vast polar structure of the milky way attains new members*, *The Astrophysical Journal* **790** (2014) 74.
- [46] D. I. Casetti-Dinescu and T. M. Girard, *Proper motion of the Draco dwarf galaxy from Subaru Suprime-Cam data*, *Mon. Not. Roy. Astron. Soc.* **461** (Sept., 2016) 271–285, [[1606.00977](#)].
- [47] J. Einasto, *On the Construction of a Composite Model for the Galaxy and on the Determination of the System of Galactic Parameters*, *Trudy Astrofizicheskogo Instituta Alma-Ata* **5** (1965) 87–100.
- [48] E. Retana-Montenegro, E. Van Hese, G. Gentile, M. Baes and F. Frutos-Alfaro, *Analytical properties of Einasto dark matter haloes*, *Astron. Astrophys.* **540** (2012) A70, [[1202.5242](#)].
- [49] E. Hayashi, J. F. Navarro, C. Power, A. R. Jenkins, C. S. Frenk, S. D. M. White et al., *The Inner structure of lambda-CDM halos. 2. Halo mass profiles and LSB rotation curves*, *Mon. Not. Roy. Astron. Soc.* **355** (2004) 794–812, [[astro-ph/0310576](#)].
- [50] M. Mateo, *The kinematics of dwarf spheroidal galaxies*, *ASP Conf. Ser.* **116** (1997) 259, [[astro-ph/9701158](#)].
- [51] M. Mateo, E. W. Olszewski, D. L. Welch, P. Fischer and W. Kunkel, *A kinematic study of the Fornax dwarf spheroidal galaxy*, *Astron. J.* **102** (1991) 914–926.
- [52] J. Binney and G. A. Mamon, *M/L and velocity anisotropy from observations of spherical galaxies, or must M87 have a massive black hole*, *Mon. Not. Roy. Astron. Soc.* **200** (July, 1982) 361–375.
- [53] J. Binney and S. Tremaine, *Galactic dynamics*. Princeton University Press, 1987.
- [54] E. L. Lokas, *Velocity dispersions of dwarf spheroidal galaxies: dark matter versus mond*, *Mon. Not. Roy. Astron. Soc.* **327** (2001) L21, [[astro-ph/0107479](#)].
- [55] J. L. Sersic, *Atlas de galaxias australes*, Observatorio Astronomico, Cordoba (1968) .
- [56] L. Ciotti, *Stellar systems following the R exp 1/m luminosity law*, *AA* **249** (1991) 99–106.

- [57] G. B. L. Neto, D. Gerbal and I. Marquez, *The specific entropy of elliptical galaxies: an explanation for profile shape distance indicators?*, *Mon. Not. Roy. Astron. Soc.* **309** (1999) 481, [[astro-ph/9905048](#)].
- [58] M. Irwin and D. Hatzidimitriou, *Structural parameters for the Galactic dwarf spheroidals*, *Mon. Not. Roy. Astron. Soc.* **277** (1995) 1354–1378.
- [59] M. G. Walker, M. Mateo, E. W. Olszewski, J. Penarrubia, N. W. Evans and G. Gilmore, *A Universal Mass Profile for Dwarf Spheroidal Galaxies*, *Astrophys. J.* **704** (2009) 1274–1287, [[0906.0341](#)].
- [60] L. Mayer, S. Kazantzidis, C. Mastropietro and J. Wadsley, *Early Gas Stripping as the Origin of the Darkest Galaxies in the Universe*, *Nature* **445** (2007) 738–740, [[astro-ph/0702495](#)].
- [61] N. F. Martin, J. T. A. de Jong and H.-W. Rix, *A Comprehensive Maximum Likelihood Analysis of the Structural Properties of Faint Milky Way Satellites*, *ApJ* **684** (Sept., 2008) 1075–1092, [[0805.2945](#)].
- [62] J.-B. Salomon, R. A. Ibata, N. F. Martin and B. Famaey, *The intrinsic ellipticity of dwarf spheroidal galaxies: constraints from the Andromeda system*, *Mon. Not. Roy. Astron. Soc.* **450** (June, 2015) 1409–1419, [[1504.02091](#)].
- [63] C. A. Vera-Ciro, L. V. Sales, A. Helmi and J. F. Navarro, *The shape of dark matter subhaloes in the Aquarius simulations*, *Mon. Not. Roy. Astron. Soc.* **439** (Apr., 2014) 2863–2872, [[1402.0903](#)].
- [64] C. Barber, E. Starkeburg, J. F. Navarro and A. W. McConnachie, *Galactic tides and the shape and orientation of dwarf galaxy satellites*, *Mon. Not. Roy. Astron. Soc.* **447** (Feb., 2015) 1112–1125, [[1410.6161](#)].